Selective Hydrogenolysis of Polyols and Cyclic Ethers over Bifunctional Surface Sites on Rhodium−Rhenium Catalysts

Mei Chia,[†] Yomaira J. Pagán-Torres,[†] David Hibbitts,[‡] Qiaohua Tan,[‡] Hien N. Pham,[§] Abhaya K. Datye,[§] Matthew Neurock,[‡] Robert J. Davis,[‡] and James A. Dumesic*,[†]

[†]Department of Chemical and Biological Engineering, University of Wisconsin-Madison, 1415 Engineering Drive, Madison, Wisconsin 53706, United States

[‡]Department of Chemical Engineering, University of Virginia, 102 Engineers' Way, Post Office Box 400741, Charlottesville, Virginia 22904-4741, United States

[§]Department of Chemical and Nuclear Engineering and Center for Microengineered Materials, University of New Mexico, MSC 01 1120, Albuquerque, New Mexico 87131-0001, United States

S Supporting Information

ABSTRACT: A ReO_x-promoted Rh/C catalyst is shown to be selective in the hydrogenolysis of secondary C−O bonds for a broad range of cyclic ethers and polyols, these being important classes of compounds in biomass-derived feedstocks. Experimentally observed reactivity trends, NH_3 temperature-programmed desorption (TPD) profiles, and results from theoretical calculations based on density functional theory (DFT) are consistent with the hypothesis of a bifunctional catalyst that facilitates selective hydrogenolysis of C−O bonds by acid-catalyzed ring-opening and dehydration reactions coupled with metal-catalyzed hydrogenation. The presence of surface acid sites on 4 wt % Rh−ReO_x/C (1:0.5) was confirmed by NH_3 TPD, and the estimated acid site density and standard enthalpy of NH_3 adsorption were $40\,\mu mol\,g^{-1}$ and $-100\,kJ\,mol^{-1}$, respectively. Results from DFT calculations suggest that hydroxyl groups on rhenium atoms associated with rhodium are acidic, due to the strong binding of oxygen atoms by rhenium, and these groups are likely responsible for proton donation leading to the formation of carbenium ion transition states. Accordingly, the observed reactivity trends are consistent with the stabilization of resulting carbenium ion structures that form upon ring-opening or dehydration. The presence of hydroxyl groups that reside α to carbon in the C−O bond undergoing scission can form oxocarbenium ion intermediates that significantly stabilize the resulting transition states. The mechanistic insights from this work may be extended to provide a general description of a new class of bifunctional heterogeneous catalysts, based on the combination of a highly reducible metal with an oxophilic metal, for the selective C−O hydrogenolysis of biomass-derived feedstocks.
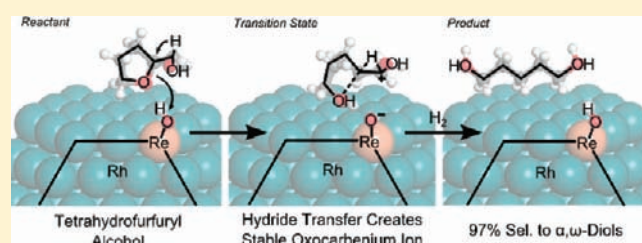
1. INTRODUCTION

A central challenge in biomass conversion lies in developing catalysts for the selective deoxygenation of highly functionalized molecules, such as sugars, polyols, and cyclic ethers, often under conditions where water is used as the solvent.[1,2] Catalytic deoxygenation may be accomplished through reactions such as decarboxylation, decarbonylation, dehydration, and C−O hydrogenolysis. Of these reactions, selective C−O hydrogenolysis of polyols and cyclic ethers over heterogeneous catalysts represents an important class of reactions for the production of high value chemicals, such as the conversion of 2-(hydroxymethyl)tetrahydropyran **1** to 1,6-hexanediol **2**. Recent experimental work suggests that platinum, ruthenium, rhodium, and iridium catalysts promoted with rhenium display not only high activity, but also high selectivity in the hydrogenolysis of tetrahydrofurfuryl alcohol **3**,[3] **1**,[4] and glycerol **4**[5−8] to their corresponding α,ω-diols. However, despite this growing body of experimental work, a systematic understanding remains elusive of the fundamental reaction mechanisms governing the rate and selectivity of C−O bond scission reactions over these interesting catalysts.

In this contribution, we first present a catalyst pretreatment strategy for obtaining a highly active and stable catalyst consisting of rhodium and rhenium supported on carbon (Rh−ReO_x/C). This catalyst is then demonstrated to be selective for the hydrogenolysis of not only **1** and **3**, but more importantly, a wide variety of C−O hydrogenolysis reactions previously unreported in the literature. Mechanistic concepts are then formulated regarding the nature of the active sites for this catalyst system for the hydrogenolysis of cyclic ethers and polyols. In this respect, it is shown that the experimental reactivity trends from this study can be understood in terms of results from density functional theory (DFT) calculations involving the deprotonation energies (DPEs) of −OH groups associated with Rh−ReO_x clusters, combined with the relative stabilities and reaction energies of carbenium structures formed by acid-catalyzed reactions and by dehydration and ring-opening activation barriers at

Table 1. Hydrogenolysis of Tetrahydrofurfuryl Alcohol 3 and 2-(Hydroxymethyl)tetrahydropyran 1 over Oxide-Promoted Rh Catalysts and Monometallic Catalysts[a]

catalyst	catalyst: reactant (g:g)	time (h)	reactant	conversion (%)	product selectivity		specific rate[b] (μmol g^{-1}min^{-1})
					compound	(%)	
4 wt % Rh—ReO$_x$/C (1:0.5)	1:9	4	3	47.2	1,5-pentanediol	97.2	180
					1-pentanol	2.8	
			1	27.3	1,6-hexanediol	97.0	90
					1-hexanol	3.0	
4 wt % Rh-MoO$_x$/C (1:0.1)	2:7	4	3	51.6	1,5-pentanediol	91.3	72
					1-pentanol	3.2	
					1-butanol	0.1	
					others[c]	5.4	
			1	25.8	1,6-hexanediol	88.6	32
					1-hexanol	3.5	
					1-pentanol	7.2	
					others[c]	0.7	
4 wt % Rh/C	2:7	4	3	8.5	1,5-pentanediol	59.1	12
					1,2-pentanediol	20.7	
					1-pentanol	7.1	
					2-pentanol	10.0	
					others[c]	3.1	
			1	3.3	1,6-hexanediol	43.5	4
					1,2-hexanediol	11.1	
					1-hexanol	2.8	
					others[c]	42.6	
3.6 wt % ReO$_x$/C	2:7	12	3	NR[d]	—	—	—
			1	NR[d]	—	—	—
1.8 wt % MoO$_x$/C	2:7	12	3	NR[d]	—	—	—
			1	NR[d]	—	—	—

[a] Reaction conditions: 393 K, 34 bar H$_2$. Feed mixtures were 5 wt % reactant in water. [b] Specific rate defined as the moles of **1** or **3** reacted per gram of catalyst per minute. [c] Alkanes in gas phase and monoalcohols at trace levels. [d] NR: no reaction.

ReOH acid sites on a model 201-atom RhRe cluster. More generally, experimental and theoretical results from this work can be extended to provide a consistent description of a class of bifunctional heterogeneous catalysts, based on the combination of a highly reducible metal with an oxophilic metal, for the selective C—O hydrogenolysis of biomass-derived feedstocks.

2. RESULTS AND DISCUSSION

2.1. Catalyst Formulation and Initial Reactivity Studies. A carbon-supported Rh catalyst was modified with two different oxophilic promoters, namely ReO$_x$ and MoO$_x$, and initial reaction kinetics studies were carried out using **1** as the reactant (Table S1, Supporting Information [SI]) to identify the amount of promoter required to maximize catalytic activity. For both promoters used, the specific activity of the promoted Rh catalysts passes through a maximum as the amount of promoter is increased. Catalysts consisting of 4 wt % Rh—ReO$_x$/C (1:0.5 atomic ratio) and 4 wt % Rh-MoO$_x$/C (1:0.1 atomic ratio) were found to be the most active materials, and these catalysts were selected for use in subsequent reaction kinetics studies.

The effect of oxophilic promoters, such as ReO$_x$ or MoO$_x$, on the C—O hydrogenolysis activities of Rh catalysts is evident in experiments with reactants **1** and **3** (Table 1). Specifically, the

hydrogenolysis rate of **3** was increased 15-fold over 4 wt % Rh—ReO$_x$/C (1:0.5) compared to the monometallic 4 wt % Rh/C catalyst. The promoting effect of MoO$_x$ is not as pronounced as for ReO$_x$: only a 6-fold increase in the hydrogenolysis rate of **3** was observed for 4 wt % Rh-MoO$_x$/C (1:0.1). Importantly, the ReO$_x$ or MoO$_x$ promoters lead to a remarkable enhancement of selectivities to the α,ω-diols for both cyclic ethers: scission of the C—O bond was observed to occur primarily at the more sterically hindered secondary carbon—oxygen bond for the promoted Rh catalysts, resulting in high selectivities to the respective α,ω-diols. This behavior is in contrast to nonselective C—O hydrogenolysis observed over monometallic 4 wt % Rh/C, as well as metal-catalyzed ring-opening of substituted cyclopentane and cyclohexane derivatives over Pt and other transition metals which preferentially occur at the least-substituted carbon—carbon bonds.[9] The increases in hydrogenolysis activity and selectivity for ReO$_x$-promoted Rh/C are in agreement with results reported by Chen, et al.[4] Experiments using monometallic 3.6 wt % ReO$_x$/C, and 1.8 wt % MoO$_x$/C catalysts indicate that the Re and Mo promoters in the absence of a highly reducible metal, such as Rh, do not possess hydrogenolysis activity, and this result is consistent with the literature.[3,4,10]

2.2. Catalyst Characterization. Temperature-programmed reduction (TPR) profiles of dried, unreduced catalysts suggest

that contact between Rh and the Re and Mo promoters is established during catalyst preparation (Figure 1), in view of the observation that the H_2 consumption peaks for 4 wt % Rh−ReO_x/C (1:0.5) and 4 wt % Rh-MoO_x/C (1:0.5) coincide with the H_2 consumption peak of monometallic 4 wt % Rh/C, in agreement with results from the literature.[11−13] These TPR profiles show that the presence of Rh lowers the reduction temperature of the Re and Mo precursors, suggesting the formation of metal alloys.[14,15] Quantitative analysis of H_2 consumption by 4 wt % Rh−ReO_x/C (1:0.5) reveals that Re is present in a highly reduced state after reduction at temperatures above 600 K: approximately 0.24 mmol H_2 was consumed compared to 0.25 mmol H_2 required to completely reduce the Rh and Re to the metallic state. The low valence of Re in 4 wt % Rh−ReO_x/C (1:0.5) after reduction with H_2 is consistent with the literature.[4,16]

High angle annular dark field scanning transmission electron microscopy (HAADF-STEM) studies of the 4 wt % Rh−ReO_x/C (1:0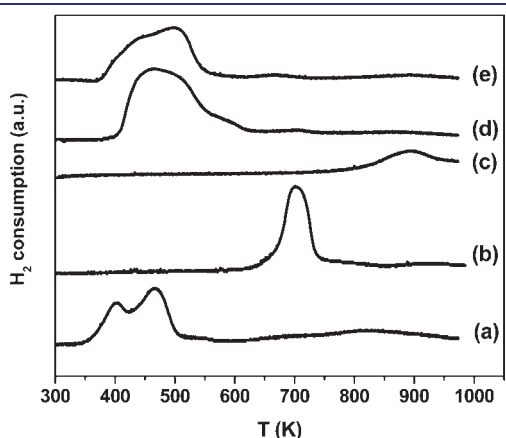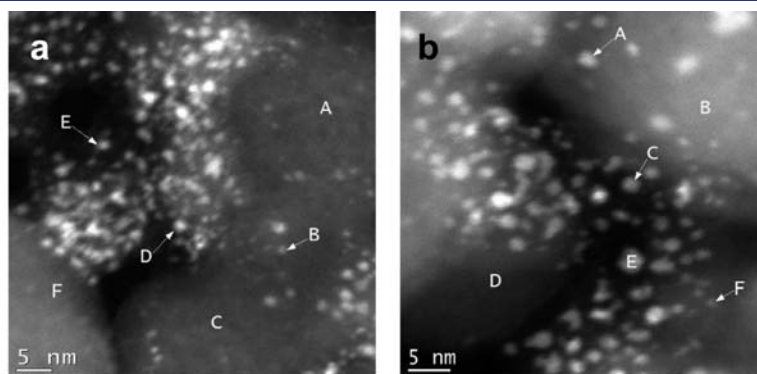.5) catalyst before and after reaction revealed that the metallic nanoparticles typically contained both Rh and Re, as seen in electron dispersive X-ray spectroscopy (EDS) micro-analyses of Figure 2. The average metallic particle size of the 4 wt % Rh−ReO_x/C (1:0.5) catalyst before and after reaction was estimated to be 2.1 nm from HAADF-STEM analysis of over 700−900 randomly selected particles, as displayed in Figure 3.

The extent of irreversible CO adsorption at 298 K on the various supported carbon catalysts was used to estimate the dispersions of the metallic particles (where dispersion is defined as the fraction of the metallic atoms that are on the surface), and these results are shown in Table 2. The metal dispersion was found to be approximately 50% for both monometallic 4 wt % Rh/C and 4 wt % Rh−ReO_x/C (1:0.5). The particle size of the as-prepared 4 wt % Rh−ReO_x/C (1:0.5) catalyst determined from metal dispersion values was found to be in the range of 2.2−2.3 nm (Table 2).

In general, estimates of the metal particle sizes obtained from HAADF-STEM and metal dispersion values compare well with one another, and indicate that no significant changes in particle size take place upon exposure to reaction conditions.

Temperature-programmed desorption (TPD) profiles for NH_3 from reduced catalysts indicate that acid sites are present on 4 wt % Rh−ReO_x/C (1:0.5) (Figure 4). All catalyst samples were pretreated in flowing H_2 at 523 K for 4 h prior to the adsorption of NH_3. As shown in Figure 5, the NH_3 desorption profile for 4 wt % Rh−ReO_x/C (1:0.5) displays a peak with maximum at 498 K. The number of acid sites on 4 wt % Rh−ReO_x/C (1:0.5) was 40 μmol g^{-1}, and number ratio of acid to metal sites was equal to 0.28. Assuming that the standard entropy change of adsorption (ΔS°_{ads}) is approximately −150 J K^{-1} mol^{-1},[20,21] which corresponds to loss of the gas-phase translational entropy, and that first-order desorption and rapid readsorption occurs, the heat of adsorption of NH_3 (ΔH°_{ads}) on 4 wt % Rh−ReO_x/C (1:0.5) can be estimated[22] to be −100 kJ mol^{-1}. In contrast, no discernible NH_3 desorption peaks were observed for monometallic 4 wt % Rh/C and 3.6 wt % Re/C under the conditions employed. The lack of acidity of Re/C here could be due to a combination of low Re loading and poor metal dispersion.

Figure 1. Temperature-programmed reduction profiles for (a) 4 wt % Rh/C, (b) 3.6 wt % Re/C, (c) 1.8 wt % Mo/C, (d) 4 wt % Rh−Re/C (1:0.5), (e) 4 wt % Rh−Mo/C (1:0.5).

Particle	Figure 2a (as-prepared)						Figure 2b (spent)					
	A	**B**	**C**	**D**	**E**	**F**	**A**	**B**	**C**	**D**	**E**	**F**
Rh (at%)	0.76	0.73	0.02	5.45	0.27	0.03	1.14	0.06	6.39	0.14	5.32	0.77
Re (at%)	0.13	0.2	0.02	1.33	0.31	0.01	0.23	0.10	4.58	0.00	0.77	0.14
Re:Rh	0.2	0.3	1.0	0.2	1.2	3.0	0.2	1.7	0.7	-	0.1	0.2

Figure 2. Representative HAADF STEM images and EDS spot-beam analysis results of (a) as-prepared and (b) spent 4 wt % Rh−ReO_x/C (1:0.5) catalysts.
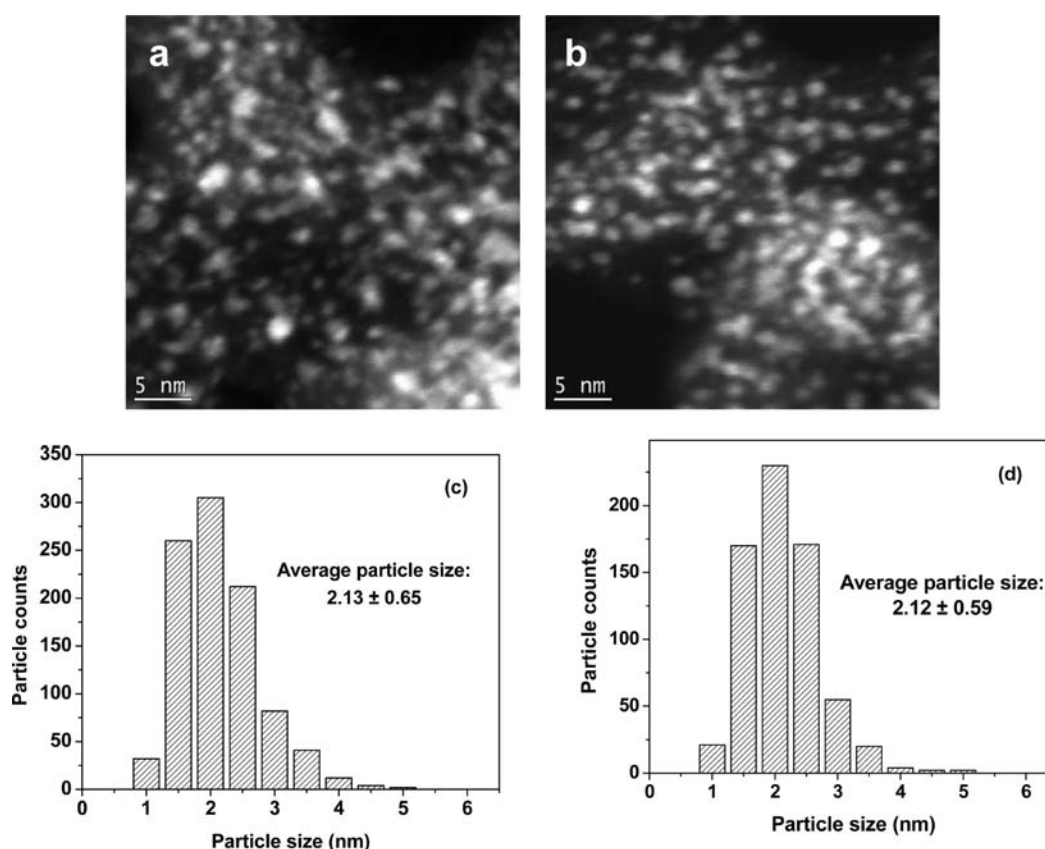
Figure 3. Representative HAADF-STEM images and particle size distribution histograms for (a, c) as-prepared and (b, d) spent 4 wt % Rh−ReO$_x$/C (1:0.5) catalysts. Number-averaged particle sizes are presented in the figures.

Table 2. Quantification of CO Adsorption on Monometallic and Promoted Rh Catalysts at 298 K

catalyst	Rh loading (wt%)	Re loading (wt%)	Rh:Re (mol:mol)	pretreatment temperature (K)	irreversible CO uptake (μmol g^{-1})	CO:Rh (mol:mol)	dispersion (%)[a]	particle size (nm)[b]
Rh/C	4	—	—	393	151	0.39	52	2.1
Re/C	—	3.6	—	723	29	0.15[c]	—	—
Rh−Re/C (as-prepared)	4	3.6	1:0.5	393	143	0.38	51	2.2
				523	145	0.39	51	2.2
				723	135	0.36	48	2.3
Rh−Re/C (spent)	4	3.6	1:0.5	393	7	0.02	—	—
				723	74	0.20	—	—

[a] Dispersion calculated with respect to total Rh loading and assuming 0.75 ML coverage of CO at full saturation. [b] Particle size = 1.1/dispersion; factor of 1.1 calculated from the literature.[17−19] [c] CO:Re.

2.3. Catalyst Pretreatment and stability. Rhenium is oxophilic and some of its oxides (e.g., Re$_2$O$_7$ and ReO$_3$) are soluble in water, leading potentially to the leaching of rhenium from the catalyst under aqueous reaction environments and to possible homogeneous catalysis. To optimize catalyst pretreatment conditions for maximum activity and stability of the 4 wt % Rh−ReO$_x$/C (1:0.5) catalyst, the effect of catalyst reduction temperature on the rate of hydrogenolysis for reactant **1** was first determined, and the extent of rhenium leaching monitored (Table S2, SI). These experiments were conducted in a batch reactor, and pretreatment of the dry catalyst was performed under H$_2$ atmosphere at temperatures of 393 and 523 K prior to addition of the aqueous feed. After reaction for 4 h at 393 K, the reactor was cooled to 298 K, the vessel was depressurized, and the reaction solution was filtered to remove the catalyst. Elemental analysis of the filtrates was performed by inductively coupled plasma atomic emission spectroscopy (ICP-AES). The results in Table S2 (SI) show that the catalytic activity and the extent of rhenium leached into the reaction solution were highest without pretreatment of the catalyst (2%) or with a low temperature pretreatment (393 K, 1%). The extent of Re leaching was substantially lower (<0.5%, which is at the detection limit of our system) after pretreatment at 523 K, and therefore, this condition was chosen for use in continuous flow experiments to further study catalyst stability versus time-on-stream.
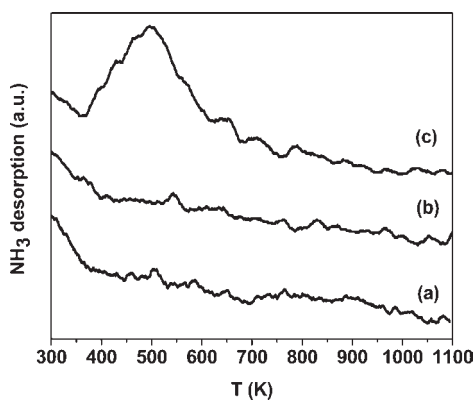
Figure 4. NH$_3$ temperature-programmed desorption profiles for (a) 3.6 wt % Re/C, (b) 4 wt % Rh/C, and (c) 4 wt % Rh—Re/C (1:0.5). Catalyst samples were pretreated in flowing H$_2$ (100 cm^3 (STP) min^{-1}) at 523 K for 4 h prior to dosing of NH$_3$.
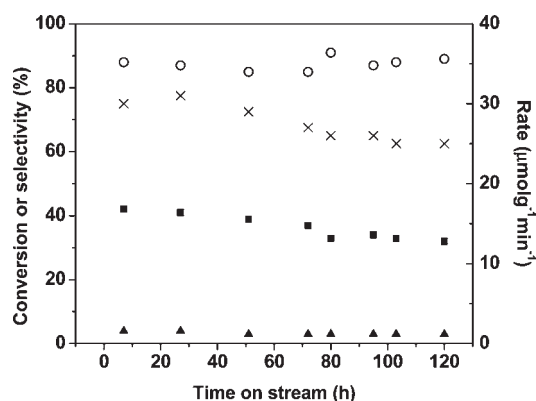

Figure 5. Results for the hydrogenolysis of 2-(hydroxymethyl) tetrahydropyran **1** over 4 wt % Rh—ReO$_x$/C (1:0.5) in a continuous flow system. Conversion of **1** (■), selectivities to 1,6-hexanediol **2** (○) and 1-hexanol (▲), and reaction rates (×) at 393 K, 34 bar H$_2$, WHSV = 0.52 h^{-1}, feed: 5 wt % **1** in water. The catalyst was pretreated in flowing H$_2$ (60 cm^3 (STP) min^{-1}) at 523 K for 4 h and cooled to the reaction temperature prior to initiation of liquid feed flow.

Figure 5 shows results for the hydrogenolysis of **1** over 4 wt % Rh—ReO$_x$/C (1:0.5) in a continuous packed-bed reactor system. The catalyst was pretreated under flowing H$_2$ for 4 h at 523 K prior to initiating the flow of liquid feed. Under these continuous flow conditions, the performance of the catalyst stabilized at conversion level of 32% and a selectivity to **2** of 90%. After 120 h time-on-stream, the activity of the catalyst declined by only 16%. The stability of the catalyst under continuous liquid flow conditions provides definitive evidence that we have established catalyst pretreatment and reaction conditions under which 4 wt % Rh—ReO$_x$/C (1:0.5) functions fully as a heterogeneous catalyst.

2.4. Hydrogenolysis of Cyclic Ethers. To better understand the high hydrogenolysis selectivities of **1** to **2** over 4 wt % Rh—ReO$_x$/C (1:0.5), the hydrogenolysis rates of cyclic ethers with different functional groups were studied in a batch reactor, and the results are shown in Table 3. The reactivity trend for the six-membered cyclic ethers was observed to be **1** ≫ 2-methyltetrahydropyran **5** > tetrahydropyran **6**. The reactivity trend of the five-membered ring cyclic ethers is analogous to that of the six-membered ring molecules, where **3** ≫ 2-methyltetrahydrofuran

7 > tetrahydrofuran **8**. For both classes of cyclic ethers, the absence of the hydroxyl group leads to a significant decrease in C—O hydrogenolysis activity. These results suggest that the hydroxyl groups in **1** and **3** are responsible for the high C—O hydrogenolysis rates and selectivities to their respective α,ω-diols over 4 wt % Rh—ReO$_x$/C (1:0.5). This selectivity toward ring-opening at the more substituted carbon center is not consistent with the preferential ring-opening of the less sterically hindered sites of substituted cyclohexane and cyclopentane intermediates over metal surfaces.[9] As is described below in regard to the ring-opening of compounds **5** and **7**, metal-catalyzed ring-opening first occurs through dehydrogenation, causing the unsubstituted sites to be preferentially activated.

We suggest instead that the experimentally observed hydrogenolysis selectivity trends are consistent with a bifunctional mechanism in which the catalyst facilitates initial acid-catalyzed ring-opening at the more substituted carbon center followed by metal-catalyzed hydrogenation. To elucidate the observed differences in reactivity and product selectivity, a quantitative measure of the reactivity of these different molecules over solid acids is needed. Accordingly, a Born cycle analysis can be used to establish a relationship between the changes in the activation barrier and changes in the catalyst or the molecules reacted. More specifically, the activation barrier (E_a) for a reaction can be written in terms of the deprotonation energy (DPE) of the acid, which provides a measure of solid acidity, the gas-phase carbenium ion reaction or formation energies ($\Delta H_{rxn(R+)}$), and the interaction energy (ΔE_{int}) between the gas-phase carbenium ion and the negative charge of the conjugate base that forms in the transition state:[23,24]

$$E_a = DPE + \Delta H_{rxn(R+)} + \Delta E_{int} \qquad (1)$$

As the catalyst is identical for all of the reactions considered in Table 3, the reactions can therefore be described by the changes in the gas-phase carbenium ion reaction energies, $\Delta H_{rxn(R+)}$, and changes in the interaction energies, ΔE_{int}. If the catalyst is the same, the changes in the interaction energies that result from different reactants are often linearly related to the changes in the proton affinity of the reactant or the gas-phase carbenium ion reaction energies.[25] The acid-catalyzed C—O activation is thought to proceed via the simultaneous protonation of the oxygen atom in the ring and ring-opening, thus resulting in the formation of a secondary carbenium which can be stabilized through a Coulombic interaction between the positive charge on the carbenium ion center and the neighboring oxygen on the hydroxyl group through a back-side interaction as shown in Figure 6. This secondary carbenium ion intermediate can rapidly undergo a hydride transfer with the neighboring —CH—OH intermediate to form the more stable RCH$_2$—C=O(+)H oxocarbenium intermediate depicted in Figure 6 which more effectively stabilizes the charge on the oxygen atom. Alternatively, the ring-opening can proceed directly with a concerted hydride transfer from the neighboring CH—OH group to form the more stable RCH$_2$—C=O(+)H intermediate. While we have calculated the reaction energies to form the oxirane (3-membered ring) and oxetene (4-membered ring) as well as the RCH$_2$—C=O(+)H oxocarbenium ions that result from the stabilization of the OH intermediates (see Table 4), we herein discuss only the results for the energetically more stable oxocarbenium ion intermediates. To further demonstrate and ensure the validity of gas-phase carbenium ion calculation results, more

Table 3. Hydrogenolysis of Cyclic Ethers and Polyols over 4 wt % Rh–ReO$_x$/C (1:0.5)[a]

Reactant Structure	Name	Reactant concentration (wt%)	Time (h)	Conversion (%)	Product selectivity Compound	(%)	Specific rate[b] (μmol g⁻¹ min⁻¹)	Specific rate/ initial reactant concentration (mL g⁻¹ min⁻¹)
	2-(hydroxymethyl) tetrahydropyran **1**	5	4	27.3	1,6-hexanediol	97.0	90	0.21
					1-hexanol	3.0		
	2-methyltetrahydropyran **5**	1	4	NR[c]	-	-	-	
		1[d]	20	33.6	2-hexanol	24.3	7	0.08
					Others[e]	75.7		
	tetrahydropyran **6**	1	4	NR[c]	-	-	-	-
	tetrahydrofurfuryl alcohol **3**	5	4	47.2	1,5-pentanediol	97.2	180	0.36
					1-pentanol	2.8		
	2-methyltetrahydrofuran **7**	5	4	1.4	2-pentanol	>99.9	7	0.01
		5[d]	20	20.5	2-pentanol	58.4	7	
					1-pentanol	1.6		
					2-butanol	2.9		
					Others[e]	37.1		
	tetrahydrofuran **8**	5	4	NR[c]	-	-	-	-
	1,2,6-hexanetriol	5	4	8.1	1,6-hexanediol	>99.9	23	0.06
		5[d]	14	59.3	1,6-hexanediol	61.9	17 (1)[f]	
					1,5-hexanediol	8.7		
					1-hexanol	3.6		
					2-hexanol	0.2		
					1-pentanol	5.0		
					2-pentanol	4.4		
					2-methyltetrahydropyran	3.5		
					Others[e]	12.7		
	1,2,4-butanetriol	5	4	13.1	1,2-butanediol	8.9	47	0.10
					1,3-butanediol	14.2		
					1,4-butanediol	62.8		
					1-butanol	5.6		
					2-butanol	3.4		
					Others[e]	5.1		
	glycerol **4**	5	4	9.8	1,3-propanediol	24.0	45	0.08
					1,2-propanediol	37.2		
					1-propanol	27.3		
					2-propanol	11.4		
		5[d,g]	12	10.5	1,3-propanediol	5.3	6	
					1,2-propanediol	17.7		
					1-propanol	8.2		
					2-propanol	68.8		
	1,6-hexanediol **2**	3	4	NR[c]	-	-	-	-
	1,2-hexanediol	3	4	12.4	1-hexanol	79.5	40	0.15
					2-hexanol	19.0		
					Others[e]	1.5		
	1,5-pentanediol **11**	3	4	1.0	1-pentanol	97.8	2	0.01
					Others[e]	2.2		
	1,2-pentanediol **13**	3	4	8.8	1-pentanol	87.8	32	0.11
					2-pentanol	12.2		
	2,4-pentanediol **15**	3	4	30.9	2-pentanol	88.9	58	0.21
					Others[e]	11.1		
	1,4-butanediol **12**	5	4	2.1	1-butanol	67.6	4 (2)[f]	0.01
					tetrahydrofuran	32.4		
	1,2-butanediol **14**	5	4	14.9	1-butanol	78.4	62	0.11
					2-butanol	21.6		
	2,3-butanediol **16**	5	4	38.3	2-butanol	80.1	78	0.15
					Others[e]	19.9		
	ethylene glycol	5	4	40.0	ethanol	95.0	116	0.15
					Others[e]	5.0		

[a] Reaction conditions: 393 K, 34 bar H$_2$, mass ratio of catalyst:reactant = 1:9. [b] Specific rate defined as the moles of reactant consumed per gram of catalyst per minute. Total specific rates are divided by two to account for symmetry in molecules **11**, **12**, **15**, **16**, and ethylene glycol. [c] NR: no reaction. [d] Mass ratio of catalyst:reactant = 2:7. [e] Alkanes in gas phase and monoalcohols at trace levels. [f] Ring-closing rate denoted in parentheses. [g] Catalyst used was 4 wt % Rh/C.

detailed analyses of the reaction paths and corresponding activation barriers were performed for the five-membered ring structures **3** and **7** over a model Rh$_{200}$Re$_1$OH cluster, as outlined below.

The results from DFT calculations for simple gas-phase carbenium ion reaction energies presented in Figure 6 and Table 4 show that the high selectivities for ring-opening **1** and **3** to the α,ω-diol can be attributed to the greater stability (30 kJ mol^{-1}) of
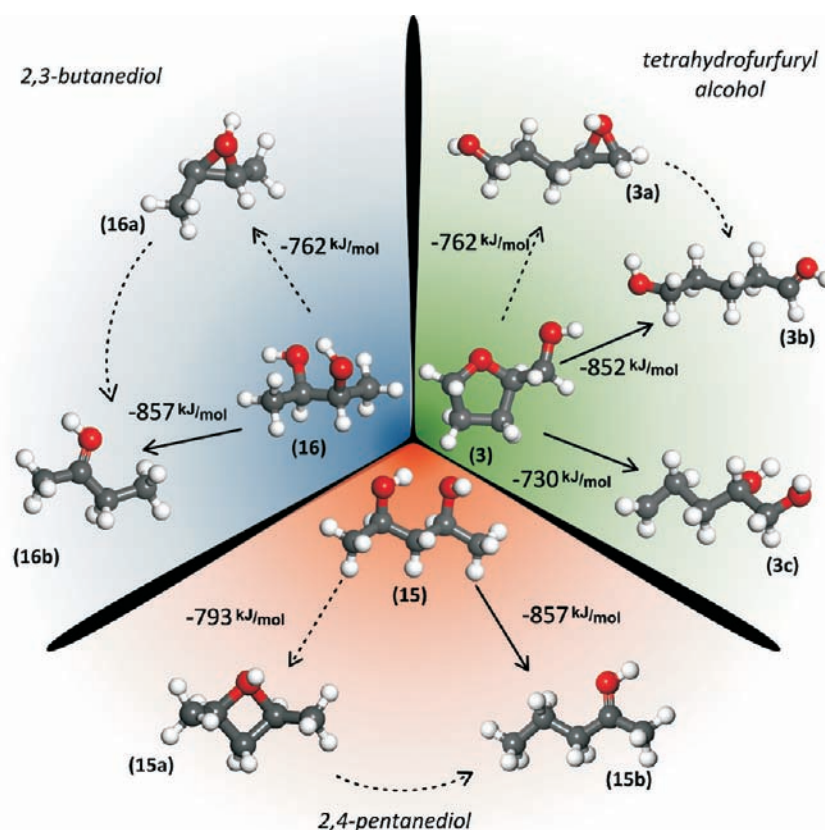
Figure 6. DFT-calculated carbenium and oxocarbenium ion formation or reaction energies for 2,3-butanediol **16**, 2,4-pentanediol **15**, and tetrahydrofurfuryl alcohol **3**. The dotted lines refer to sequential paths which proceed via the formation of the OH-stabilized three (oxirane) and four (oxetene) ring intermediates that subsequently form the corresponding oxocarbenium ion intermediates, whereas the solid lines refer to concerted protonation/hydride transfer steps that result in the direct formation of the oxycarbenium ion intermediates.

the secondary carbenium ion structures leading to the α,ω-diol, versus the primary carbenium ion structures which result in the formation of the 1,2-diol. Furthermore, the presence of a hydroxyl group at the α or β position allows for the concerted protonation and hydride transfer to form the more stable oxocarbenium $(RCH_2-CH=O(+)H)$ ion intermediate. For cyclic ethers, the presence of the hydroxyl substituent α to the dehydration center is shown to increase the stability of the carbenium ion, such that the carbenium ion formation energies for **1** and **3** are -845 and -852 kJ mol^{-1}, respectively, while the corresponding structures without the $\alpha-$OH substituent, **5** and **7**, are significantly less stable at -742 and -743 kJ mol^{-1}, respectively (Figure 6 and Table 4). This trend was confirmed by more rigorous transition state simulations over model $Rh_{200}Re_1OH$ clusters, displayed in Figure 7, which show that the activation barrier to ring-open **3** (Figure 7A) is lower by 14 kJ mol^{-1} compared to the barrier to open **7** (Figure 7C) as a result of the back-side stabilization of the positive charge in the carbenium ion transition state by the OH group and by stabilization with water. The concerted protonation and hydride transfer reaction to form the oxocarbenium ion transition state lowers the activation barrier by an additional 16−84 kJ mol^{-1} as shown in the Results displayed in Figure 8. While these calculations explain the selectivities reported in Table 3, the absolute values of the activation barriers are likely overpredicted due to the simplicity of the model system; both the presence of water and acid sites stronger than those in the modeled system would lead to lower activation barriers.

The ring-opening of cyclic ethers **5** and **7** is characteristically different from the functionalized cyclic structures discussed above, in that the C−O activation occurs at the sterically less-hindered primary carbon−oxygen bond, leading to the formation of the corresponding secondary alcohols (i.e., 2-hexanol **9** and 2-pentanol **10**, respectively). This preferential hydrogenolysis of **7** at the primary carbon−oxygen bond is similar to that observed by Gennari, et al. who performed gas-phase reactions over unpromoted Pt catalysts.[26,27] The activation of the ring for these cyclic ethers, however, cannot be explained through acid chemistry, as it would result in the formation of a highly unstable primary carbenium ion. Instead, these experimental trends are consistent with DFT results for ring-opening of cyclic ethers via a solely metal-catalyzed route over Rh (Figure 9), showing that metal-catalyzed insertion is favored at the less substituted C−O bond by 30 kJ mol^{-1} due to steric hindrance at the substituted C−O bond, preventing the initial dehydrogenation which leads to C−O cleavage.

2.5. Hydrogenolysis of Polyols. To study further the role of hydroxyl groups in the hydrogenolysis of neighboring C−O bonds, the reactivity profiles for several straight-chain polyols over the 4 wt % Rh−ReO$_x$/C catalyst were examined, and these results are shown in Table 3. For all diols studied, it is apparent that 1,2-diols are more reactive than α,ω-diols. Furthermore, the selectivity is significantly higher toward hydrogenolysis of the hydroxyl group at the secondary carbon atom for all 1,2-diols, leading to the formation of the corresponding primary alcohol as

Table 4. DFT Calculated Gas-Phase Reaction Energies for the Formation of Carbenium and Oxocarbenium Ion Intermediates Involved in the Ring-Opening of Cyclic Ethers and Dehydration of Polyols

Reactant Structure	Name	Carbenium Ion Formation or Reaction Energy (kJ/mol)	Carbenium Ion Structure
	2-(hydroxymethyl)tetrahydropyran 1	-845	
		-756	
		-714	
	2-methyltetrahydropyran 5	-742	
		-710	
	tetrahydropyran 6	-710	
	tetrahydrofurfuryl alcohol 3	-852	
		-760	
		-730	
	2-methyltetrahydrofuran 7	-743	
		-731	
	2,4-hexanediol	-857	
		-799	
	1,2-pentanediol 13	-833	
		-741	
	2,3-pentanediol	-857	
		-770	
	2,4-pentanediol 15	-857	
		-794	
	1,2-butanediol 14	-830	
		-736	
	2,3-butanediol 16	-857	
		-762	
	1,2-propanediol	-826	
		-730	
	1,3-propanediol 17	-826	
		-736	
	glycerol 4	-810	
		-730	
	ethylene glycol	-822	
		-707	

the predominant product. The high reactivity for hydrogenolysis of a secondary hydroxyl group adjacent to a primary hydroxyl group is also exhibited in the reactivity trends of the triols. In addition, a secondary hydroxyl group in close proximity to another secondary hydroxyl group shows high reactivity for undergoing hydrogenolysis over 4 wt % Rh—ReO$_x$/C (1:0.5). These reactivity trends show that the position of hydroxyl groups in a reactant molecule is instrumental in dictating its hydrogenolysis reactivity over 4 wt % Rh—ReO$_x$/C (1:0.5).

As previously shown for cyclic ethers, the above experimental trends for polyols are also consistent with a bifunctional catalyst which facilitates initial acid-catalyzed carbenium ion chemistry followed by metal-catalyzed hydrogenation. The low hydrogenolysis rates of α,ω-diols **2**, 1,5-pentanediol **11**, and 1,4-butanediol **12** are in agreement with the lower stability of primary carbenium ions which would form upon dehydration of these

reactants. The higher reactivity and selective hydrogenolysis of 1,2-diols, such as 1,2-pentanediol **13** and 1,2-butanediol **14**, at the secondary C—O bond can be explained by the formation of the more stable RCH$_2$—CH=O(+)H oxocarbenium ion intermediates resulting from the concerted elimination of water and hydride transfer from the primary —CH$_2$OH group, as reported in Table 4. Additionally, the higher reactivities of β-diols such as 2,4-pentanediol **15** and 2,3-butanediol **16** over that for 1,2-diols can be similarly explained by the formation of the secondary oxocarbenium ions in **15b** and **16b** which are more than 100 kJ mol^{-1} more stable than the secondary carbenium ions in **15a** and **16a**.

2.6. Governing Principles of Substrate Reactivity and Selectivity. The experimental reactivity and selectivity trends shown in Table 3 are in agreement with the carbenium ion formation energies presented in Table 4. The reactants studied
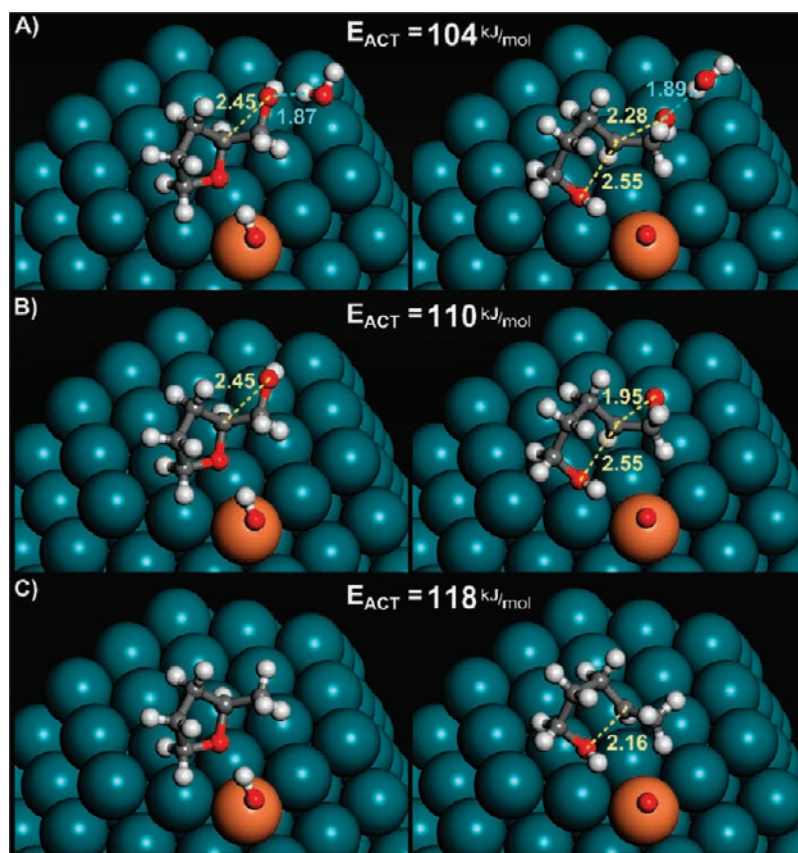
Figure 7. DFT-calculated reactant and transition state structures and corresponding activation barriers for the acid catalyzed ring-opening of: (a) water-stabilized tetrahydrofurfuryl alcohol **3**, (b) tetrahydrofurfuryl alcohol **3** and (c) 2-methyltetrahydrofuran **7** on a model $Rh_{200}Re_1OH$ cluster.
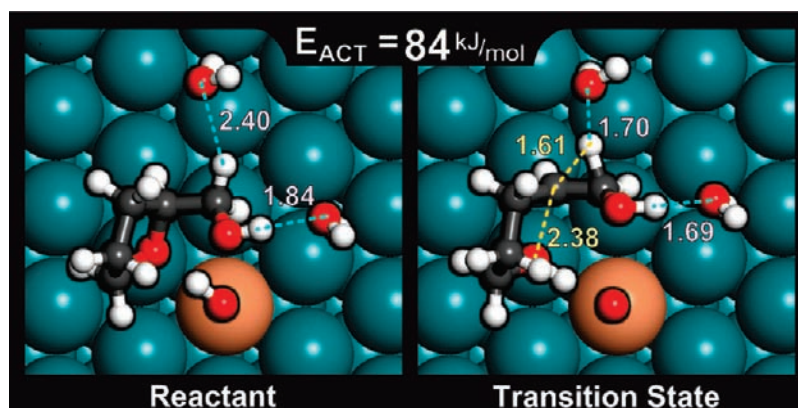

Figure 8. DFT-calculated reactant and transition state structures for the concerted protonation, hydride transfer and ring-opening of the water-stabilized tetrahydrofurfuryl alcohol **3** over a model Rh(111) surface with well dispersed Re−OH sites.

are ranked from the most to the least reactive in Table S3 (SI), along with their corresponding carbenium ion reaction energies. The results indicate that the most reactive molecules are the cyclic ethers which contain hydroxyl substituents that are located α to the carbon atom in the C−O bond where the ring is opened. These reactants can undergo concerted ring-opening and hy-dride transfer from the neighboring −CH$_2$OH group to form stable primary oxocarbenium ion transition state structures which are further stabilized by the OH groups that result upon protonation of the ring. As such, structures **1** and **3** are two of the

most reactive structures examined with specific reaction rates of 90 and 180 μmol g^{-1} min^{-1}, respectively.

β-Diols (**15** and **16**) also lead to stable oxocarbenium ion structures that can effectively stabilize the carbenium ion charge that results upon dehydration. These structures appear to be just as reactive as those for **1** and **3** with specific rates of 58 (**15**) and 78 (**16**) μmol g^{-1} min^{-1}. In agreement with this experimental finding, the theoretical results show similar carbenium ion forma-tion energies. The structures of carbenium ions from linear polyols with α,β−OH groups are less stable, as the oxocarbenium ions

that form are now delocalized over primary carbon atoms in the oxocarbenium ion structure without the additional OH stabilization in the transition state; the reactivities of these reactants lie between 23 and 62 μmol g^{-1} min^{-1}. Linear polyols that do not contain α,β or $\beta,\beta-$OH substituents are unable to form oxocarbenium ion structures and must effectively stabilize the charge on the secondary carbon centers. As such the reactivities of these reactants are significantly lower and found to be in the range of 10 μmol g^{-1} min^{-1}. Finally, all of the primary carbenium ion centers from linear and cyclic polyols are unstable, and as such these reactants do not show significant reactivity.

The results from Table S3 (SI) (with the exception of the data for the ring-opening of **5** and **7** which are metal-catalyzed reactions, and data from the unreactive α,ω-polyols) are plotted in Figure 10, showing a correlation between the carbenium ion formation energy and the logarithm of the normalized rate
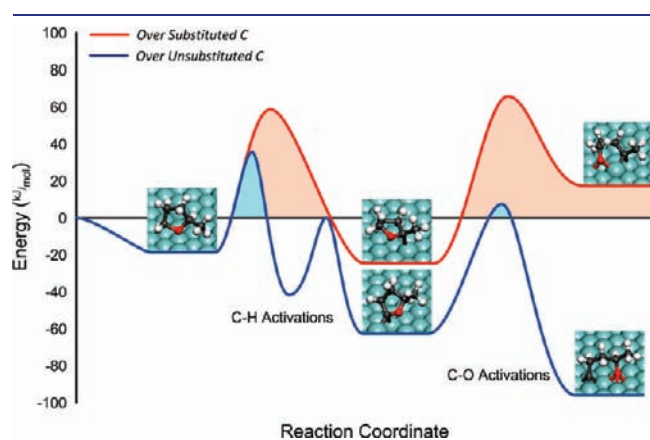

Figure 9. DFT-calculated reaction path and energies for the metal-catalyzed ring-opening of 2-methyltetrahydrofuran **7** at the substituted and unsubstituted carbon centers over Rh.

expressed as the ratio between specific reaction rate (μmol g^{-1} min^{-1}) and initial reactant concentration (μmol mL^{-1}). This ratio is employed to reflect an appropriately normalized reaction rate which is independent of the minor differences in the initial molar concentrations of reactants (see below). It is also notable that specific rate values were divided by two to account for molecules with a plane of symmetry, namely, **11**, **12**, **15**, **16**, and ethylene glycol. The differences in reactivity between unsubstituted (primary carbenium ions), substituted (secondary), and substituted and OH-stabilized cyclic ethers and polyols are highlighted by different colored regions in Figure 10.

We note here that we have included glycerol in the correlation of Figure 10, showing that the overall reactivity for conversion of this molecule is controlled by acid catalysis, consistent with the high selectivity for the formation of 1,3-propanediol **17**, compared with the metal-catalyzed route over Rh/C. It is interesting that the rate of formation of 1,2-propanediol over the Rh$-$ReO$_x$/C catalyst is also much higher than the corresponding reaction over Rh/C, suggesting that an acid-catalyzed pathway exists involving a secondary carbenium ion along the way to form the 1,2 oxirane that can subsequently react to form both 1,2 and 1,3 propanediol products close to the relative percentages that are seen experimentally.

2.7. Reaction Kinetics. Although it was impractical to evaluate the complete reaction rate expression for all 15 of the different substrates in Table 4, we evaluated the reaction kinetics for our prototypical cyclic ether, 2-(hydroxymethyl)tetrahydropyran (compound **1**), and made the reasonable assumption that other substrates in this study will behave similarly. Importantly, we used a continuous flow reactor for this study to eliminate any possible complications that could be caused by initial transient phenomena (e.g., catalyst deactivation, initial leaching of rhenium) that could take place in a batch reactor. The results of these flow reactor studies, presented in Table S4 (SI), show that the reaction is approximately first order with respect to species **1** and slightly less than first order (i.e., approximately equal to 0.9) with
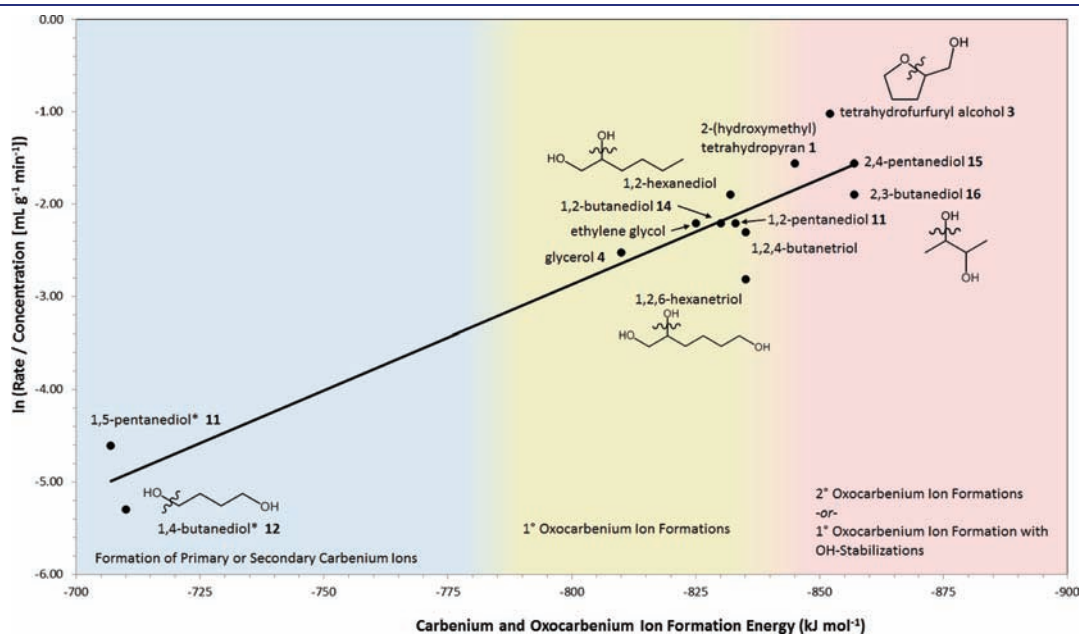

Figure 10. Comparison of the normalized rate, defined as the ratio between specific reaction rate (μmol g^{-1} min^{-1}) and initial reactant concentration (μmol mL^{-1}) (on a logarithmic scale), and DFT-calculated carbenium and oxocarbenium ion energies for selected cyclic ethers and linear polyols. Each region shows distinct shifts in activity due to the stability of the carbenium and oxocarbenium ions as discussed in Table S3 (SI).
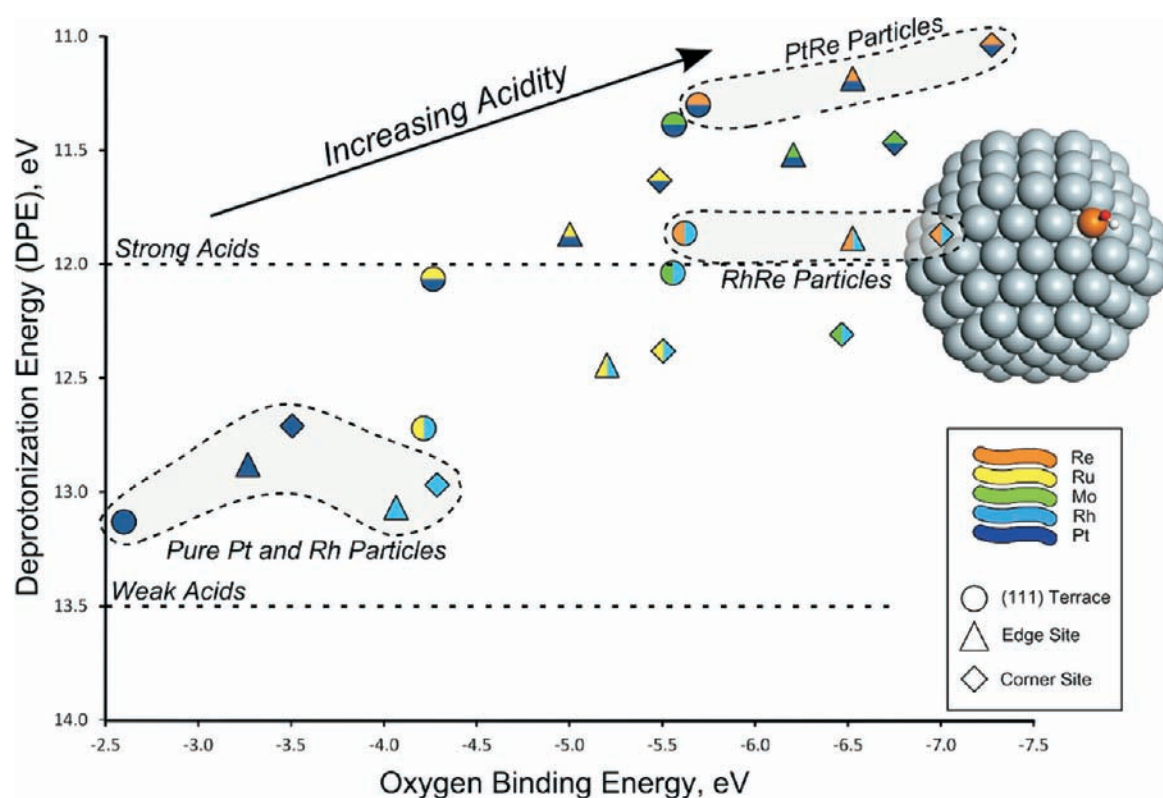
Figure 11. DFT-calculated deprotonation energies for various surfaces and atom clusters.

respect to hydrogen pressure. Because the reactivity trends of this paper indicate that acid sites must be involved in a kinetically significant part of the overall reaction scheme, one might have expected the reaction to be zero order in hydrogen. However, the observed positive order is consistent with the bifunctional nature of the catalyst and the complexity of the mechanism, as illustrated by Boudart and Djega-Mariadassou in studies of the influence of hydrogen on the kinetics for isomerization of n-pentane to isopentane over a bifunctional Pt/alumina catalyst (containing metal sites and acid sites), even though hydrogen does not appear in the overall stoichiometric equation of alkane isomerization.[28] In that example, the rate determining step is the acid-catalyzed isomerization of n-pentene to i-pentene, and the observed effect of the hydrogen pressure is caused by the equilibrium of n-pentane with n-pentene on the metal sites prior to the rate determining acid-catalyzed isomerization step. In our case, we observed positive order in hydrogen resulting from the required hydrogenation of an unsaturated intermediate after the acid-catalyzed ring-opening step. In addition, it is possible that a positive effect of the hydrogen pressure is also caused by the hydrogenation of Re=O species to form the acidic Re—OH groups that are required for the overall reaction.

In summary, a simple first order reaction rate constant cannot be calculated for the reactions in this paper since they occur over a bifunctional catalyst containing acid sites and metal sites, both of which contribute to the overall reaction. However, because the reaction appears to be approximately first order with respect to the concentration of the organic reactant, we have instead chosen to correlate observed rates divided by the reactant concentration, to approximate the rate at nearly identical experimental conditions. The trend in Figure 10 of this normalized rate versus the calculated carbenium ion formation energies is surprisingly good,

given the fact that rates vary by more than an order of magnitude across the series of compounds.

2.7. Role of Rhenium and Nature of the Active Site. We suggest that the importance of acid chemistry over the rhodium—rhenium catalyst originates from the Brønsted acidity of hydroxylated Re atoms on Rh—Re nanoparticles, arising from strong Re—O bonds, resulting in a weak O—H bond as well as high electron affinity for the conjugate base. Other solid acids such as zeolites[23] and heteropolyacids (HPAs)[29] achieve this high electron affinity through the distribution of the negative charge across multiple oxygen atoms. As shown in Figure 11, hydroxylated rhenium species on Rh—Re nanoparticles demonstrate deprotonation energies at the corner, edge and terrace sites of 1140 kJ mol^{-1}, as compared to values of 1050—1200 kJ mol^{-1} for well-known solid acids such as zeolites[23] and HPAs.[29] A more detailed analysis of the electronic structure shows that there is electron transfer from Re to the oxygen. Also, it is evident from Figure 11 that the DFT-predicted acidities of hydroxylated molybdenum species on Rh—Mo nanoparticles are markedly lower than that for Rh—Re, consistent with the lower hydrogenolysis rates observed of **1** over the 4 wt % Rh-MoO$_x$ (1:0.1) catalyst (Table 1). Further experimental evidence of the presence of surface acid sites on the Rh—Re catalyst is provided by results from NH$_3$ TPD studies (Figure 4) which show that the acid site density over this catalyst is approximately 40 μmol g^{-1}. Additionally, we found that the hydrogenolysis of **1** over monometallic Rh/C in the presence of 0.1 M H$_2$SO$_4$ or HCl proceeds at rates and selectivities to **2** which are significantly lower than that over RhReO$_x$/C (Table 5). The above results thus suggest that the active sites for RhReO$_x$/C are located at the catalyst surface in the form of hydroxylated rhenium near rhodium.

Table 5. Effect of Homogeneous Acid and Base on Hydrogenolysis Rate and Product Selectivity of 2-(Hydroxymethyl)-tetrahydropyran 1 over Rh-Containing Catalysts[a]

catalyst	time (h)	conversion (%)	selectivity to 1,6-hexanediol 2 (%)	selectivity to 1,2-hexanediol (%)	specific rate[b] (μmol g^{-1} min^{-1})
4 wt % Rh—ReO$_x$/C (1:0.5)	4	27	97	0	90
4 wt % Rh—ReO$_x$/C (1:0.5) and 0.1 M NaOH	4	NR[c]	—	—	—
4 wt % Rh/C	20	NR[c]	—	—	—
4 wt % Rh/C and 0.1 M H$_2$SO$_4$	20	13	41	1	9
4 wt % Rh/C and 0.1 M HCl	20	6	32	7	4
4 wt % Rh/C and 0.1 M NaOH	20	NR[c]	—	—	—

[a] Reaction conditions: 393 K, 34 bar H$_2$, mass ratio of catalyst: **1** = 1:9. Reactant mixtures were 5 wt % **1** in water. [b] Specific rate defined as the moles of **1** reacted per gram of catalyst per minute. [c] NR: no reaction

We propose that the bifunctional nature of the RhReO$_x$/C catalyst described above can be generalized to other transition metal catalysts containing rhenium. For example, we have recently reported the promotion of the hydrogenolysis of **4** on Re-promoted Pt catalysts.[8] In that work, addition of Re to the Pt catalyst increased the turnover frequency of the hydrogenolysis of **4** by a factor of 20, with **17** now appearing in the product mixture. Indeed, the selectivity of the hydrogenolysis reaction to **17** over Pt—Re was 34% at 443 K, a temperature at which Pt alone exhibited only trace conversion of glycerol.

Similarly, we observe here that the hydrogenolysis of **4** over 4 wt % Rh—Re/C (1:0.5) resulted in a marked increase in hydrogenolysis rates and selectivities to **17** compared to the performance of monometallic 4 wt % Rh catalyst (Table 3). The higher selectivities to **17** in the presence of rhenium are consistent with the premise that monometallic Pt or Rh are only able to facilitate metal-catalyzed C—O scission, while the addition of rhenium results in a bifunctional catalyst which is also capable of acid chemistry. King, et al.[30] suggested the possible formation of acid sites associated with the presence of ReO$_x$ clusters in PtRe/C catalysts, and they suggested the possible influence of these species in the aqueous phase reforming of glycerol. The basis of this proposed acidity over Pt—Re catalysts is clearly demonstrated by the DFT data presented in Figure 11, wherein Pt—Re nanoparticles are shown to display acidities comparable to that for Rh—Re nanoparticles, suggesting that similar acid-catalyzed chemistry would be displayed in both systems.

Our proposed reaction scheme involving acid-catalyzed dehydration at the secondary carbon of a polyol, followed by hydrogenation to form the α,ω-diol, is consistent with the experimental result that the presence of NaOH completely suppressed the hydrogenolysis activity of **1** over 4 wt % Rh—ReO$_x$/C (1:0.5) (Table 5). Also, previous work involving the hydrogenolysis of **4** over PtRe showed that addition of NaOH led to suppression of **20** formation.[8] Other investigators have also shown that promotion of Rh[31] or Ru[32] with Re enhances the formation of **17** from **4** in neutral water. Moreover, examination of the L$_{III}$ edge of Re in PtRe[8] as well as RhRe[31] bimetallic catalysts for the hydrogenolysis of **4** confirmed that Re is not reduced entirely to the metallic state after mild reduction in H$_2$, but instead remains in a partially oxidized state.

Finally, we note that it is possible to destroy the active sites for Rh—ReO$_x$/C catalysts by reduction in H$_2$ at elevated temperatures. In particular, the results in Figure 1 from temperature programmed reduction studies indicate that the Rh and Re in the Rh—ReO$_x$/C catalyst are both highly reduced at temperatures above about 600 K. In addition, we have found that the catalytic activity of Rh—ReO$_x$/C decreases when the catalyst is pretreated in flowing H$_2$ at increasing temperatures. These results again indicate that the active sites contain oxygen species associated with the oxophilic Re promoter of the Rh—ReO$_x$/C catalyst. We note here that we have chosen a pretreatment temperature in H$_2$ of 523 K for the Rh—ReO$_x$/C catalyst in our studies (see Figure 5), as a compromise between retaining oxygen species associated with Re and also preventing leaching of highly oxidized Re species into the aqueous solution during reaction.

3. CONCLUSIONS

We have demonstrated in this work that a ReO$_x$-promoted Rh/C catalyst is selective for the hydrogenolysis of secondary C—O bonds for a broad range cyclic ethers and polyols. It is also shown that a catalyst pretreatment strategy of reducing the catalyst in H$_2$ at 523 K prior to contact with the aqueous reactant results in the attainment of high catalytic activity and stability in a continuous flow reaction system. Importantly, results from experimentally observed reactivity trends, NH$_3$ TPD, and DFT calculations are consistent in supporting the hypothesis of a bifunctional catalyst which facilitates acid catalyzed ring-opening and dehydration coupled with metal-catalyzed hydrogenation. The presence of surface acid sites on 4 wt % Rh—ReO$_x$/C (1:0.5) has been confirmed by NH$_3$ TPD, and indicates that the acid site density and standard enthalpy of NH$_3$ adsorption are approximately 40 μmol g^{-1} and −100 kJ mol^{-1}, respectively. Results from DFT calculations show that hydroxyl groups on rhenium associated with rhodium are acidic, thus enabling proton donation to reactant molecules and formation of carbenium ion transition states. The observed reactivity trends and DFT calculations are also consistent with the enhancement in stability of carbenium and oxocarbenium ion structures that form as a result of protonation and concerted protonation and hydride transfer steps, respectively. The experimentally obtained rates of hydrogenolysis can be correlated with DFT-calculated carbenium ion formation energies. Results from this study provide the first consistent account for the bifunctional nature of active sites in metal catalysts promoted with oxophilic additives for hydrogenolysis reactions, providing guidance for the use of this class of heterogeneous catalysts for the selective deoxygenation of biomass to fuels and chemicals.

4. METHODS AND MATERIALS

Catalyst Preparation. Catalysts were prepared by incipient wetness impregnation of Vulcan XC-72 with aqueous solutions of RhCl$_3$,

NH_4ReO_4, and $(NH_4)_6Mo_7O_{24} \cdot 4H_2O$. Rh/C catalysts with oxophilic additives were obtained by successive impregnation of dried, unreduced Rh/C with the corresponding precursor of the oxophilic additive. The loading amount of the second metal is stated as a atomic ratio (e.g., 4 wt % Rh−ReO_x/C (1:0.5) catalyst designates a metal atomic ratio of Rh: Re = 1:0.5). Prior to use in experiments, catalysts were dried in air (393 K), reduced in flowing H_2 (723 K), and passivated with flowing 2% O_2 in He (298 K). Reduced and passivated catalysts are described as "as-prepared" catalysts in this paper.

CO Adsorption. Prior to CO adsorption measurements, catalysts were pretreated in 150 cm^3(STP) min^{-1} flowing H_2 at 393, 523, or 723 K for 4 h. The CO adsorption uptakes at 298 K were measured on a standard gas adsorption apparatus described elsewhere.[33]

Temperature-Programmed Reduction and NH_3 Desorption. Temperature−programmed experiments were carried out using an apparatus comprising of a tube furnace connected to a variable power-supply and PID temperature controller (Love Controls) with a K-type thermocouple (Omega). For temperature-programmed reductions, the reducing gas consisted of 5% H_2 in He, at a flow-rate of approximately 15 cm^3(STP) min^{-1}. Dried, unreduced catalyst samples (0.2 g) were loaded into a 12.6 mm outer diameter, fritted quartz tube, purged with the reducing gas for 30 min, followed by initiation of a temperature ramp at 10 K min^{-1} to 973 K. For NH_3 temperature-programmed desorption studies, reduced and passivated catalyst samples (0.4 g) were loaded into the fritted quartz tube, pretreated in flowing H_2 (100 cm^3(STP) min^{-1}) at 523 K for 4 h, and purged with He (200 cm^3(STP) min^{-1}) at 523 K for 90 min. NH_3 adsorption was performed at 298 K using 1% NH_3 in He at a flow-rate of 100 cm^3(STP) min^{-1}. After NH_3 adsorption, the sample was purged with flowing He (200 cm^3(STP) min^{-1}) at 298 K for 90 min. The He flow-rate adjusted to approximately 30 cm^3(STP) min^{-1} followed by initiation of a temperature ramp at 10 K min^{-1} from 298 to 1073 K. The effluent from the reactor tube was introduced into a vacuum chamber (5×10^{-5} Torr) via a constricted quartz capillary, and the composition of the gas was monitored by a mass spectrometer system (quadruple residual gas analyzer, Stanford Instruments RGA 200). Vacuum for the mass spectrometer was provided by a diffusion pump connected in series to a rotary pump. The NH_3 desorption profiles reported are based on the mass 15 (NH) signal which was verified to be directly indicative of NH_3 desorption alone and did not experience any interference from the fragmentation of contaminants such as H_2O and CO_2.

Electron Microscopy. Catalysts were dispersed in ethanol and mounted on holey carbon grids for examination in a JEOL 2010F 200 kV transmission electron microscope equipped with Oxford Energy Dispersive Spectroscopy (EDS) system for elemental analysis. Images were recorded in high angle annular dark field (HAADF) mode with a probe size of 1.0 nm.

Spent Catalyst Samples. All spent catalyst samples were obtained from batch reactor measurements for the hydrogenolysis of **1** (393 K, 34 bar H_2, 4 h, mass ratio of catalyst:**1** = 1:9). Reaction mixtures were filtered immediately after cooling and depressurization of the reactor. Catalyst samples were vacuum-dried at room temperature prior to use.

Batch Reactor Studies. Reactions were carried out using a 50 mL pressure vessel (Hastelloy C-276, model 4792, Parr Instrument). After loading the reactant solution, catalyst, and magnetic stirrer bar into the reactor, the vessel was sealed, purged with 34 bar He, and pressurized with H_2 (34 bar). Mechanical stirring was maintained using a magnetic stirrer plate (500 rpm).

Catalyst Pretreatment in Batch Reaction Studies. Pretreatment of the dry catalyst with H_2 was carried out at temperatures of 393 and 523 K for 12 h. Reduced and passivated dry catalyst was pretreated in a 50 mL pressure vessel (Hastelloy C-276, Model 4792, Parr Instrument) under H_2 atmosphere (34 bar) at the stipulated pretreatment temperature. The reactor was then cooled to the reaction temperature

(i.e., 393 K), the aqueous reactant mixture pumped into the vessel using a HPLC pump (LabAlliance, Series 1), and mechanical stirring of the reaction mixture initiated.

Continuous Flow Reaction Experiments. The flow reactor was a 6.4 mm (0.25 in.) outer diameter stainless steel tube with wall thickness of 0.7 mm (0.028 in.). The catalyst bed consisted of reduced and passivated catalyst (0.35 g) loaded between a quartz wool plug and fused SiO_2 granules (−4 + 16 mesh, Sigma-Aldrich). The reactor was heated with a furnace composed of close-fitting aluminum blocks externally heated by an insulated furnace (1450 W/115 V, Applied Test Systems series 3210), and temperature was monitored using a K type thermo-couple (Omega) placed outside the reactor immediately next to the position of catalyst bed. Temperature was controlled with a PID temperature controller (Love Controls, series 16A). Liquid feed solution was introduced into the reactor with cofeeding of H_2 in an up-flow configuration. A HPLC pump (LabAlliance, series 1) was used to control the liquid feed rate. Gas flow was controlled with a mass-flow controller (Brooks 5850 model), and the system pressure was maintained at 34 bar by passing the effluent gas stream through a back-pressure regulator (GO Regulator, model BP-60). The effluent liquid was collected in a gas−liquid separator and drained periodically for analysis by HPLC. Carbon balances closed within 5% for all data points.

Analytical Methods. Quantitative analyses were performed using a Waters 2695 separations module high performance liquid chromatography instrument equipped with a differential refractometer (Waters 410), a photodiode array detector (Waters 996), and an ion-exclusion column (Aminex HPX-87H, 300 mm × 7.8 mm). 0.005 M H_2SO_4 at a flow-rate of 0.6 mL min^{-1} was used as the mobile phase. Gas-phase products from batch reactions were collected in a gas bag and analyzed using a Varian GC (Saturn 3) equipped with a FID detector and a GS-Q column (J&W Scientific). The presence of rhenium in solution was detected using inductively coupled plasma atomic emission spectrometry (ICP-AES).

Density Functional Theory Calculations. All gas-phase energies were calculated using gradient-corrected DFT calculations as implemented in DMol.[3,14,34,35] Wave functions were represented by numerical basis sets of double numerical quality (DNP) with d-type polarization functions on each atom and expanded out to a 3.5 Å cutoff. The Perdew−Wang 91[36](PW91) form of generalized gradient approximation (GGA) was used to model gradient corrections to the correlation and exchange energies. The electronic density for each self-consistent iteration converged to within 1×10^{-5} au. The energy in each geometry optimization cycle was converged to within 2×10^{-5} Hartree with a maximum displacement and force of 4×10^{-3} Å and 3×10^{-3} Hartree/Å, respectively.

The gas-phase carbenium ion reaction or formation energies were calculated for ring structures as:
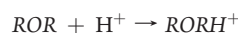
$$ROR + H^+ \rightarrow RORH^+$$

where ROR and $RORH^+$ refer to the initial ring structure and the ring-opened carbenium ion. The energies for the linear polyols, however, result in dehydration and, as such, were calculated as:

$$ROH + H^+ \rightarrow RH^+ + H_2O$$
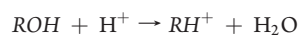
where ROH and RH^+ refer to the initial polyol and the resulting dehydrated carbenium ion. Molecules which contained neighboring α or β OH substituents were found to preferentially undergo a concerted protonation and hydride transfer to stabilize the resulting product:

$$R-CH_2OH-CH_2OH \rightarrow [R-CH(+)-CH_2OH]$$
$$\rightarrow R-CH_2-CH{=}O(+)H$$
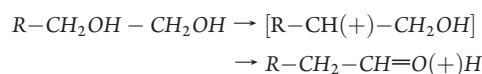
The gas-phase carbenium ion energies are used herein only as an initial probe of the activity and selectivity of the different molecules

examined experimentally. This approach oversimplifies the environment of the metal in solution. While the presence of the aqueous solution will clearly lower the overall reaction energies and activation barriers, we do not believe that selectivity patterns reported here will be altered.

All calculations on the metal surfaces and metal clusters were performed using gradient-corrected periodic plane wave DFT calculations as implemented in the Vienna Ab Initio Simulation Program (VASP).[37−39] The PW91 form of the GGA was used to determine gradient corrections to the exchange and correlation energies. Wave functions were constructed by expanding a series of plane waves within a cutoff energy of 400 eV where interactions between the core and valence electrons were modeled using Vanderbilt ultrasoft pseudopotentials.[40] For periodic calculations, a $4 \times 4 \times 1$ Monkhorst−Pack k-point mesh[41] was used to sample the first Brillouin zone, for the calculations on the metal cluster, only the Γ-point was used. The electronic energies converged to within 1×10^{-4} eV and forces on each atom were optimized to within 0.05 eV Å^{-1}. The 111 surfaces were modeled using a 3×3 unit cell with four metal layers and 16 Å vacuum region between each slab where the top two layers were allowed to relax and the bottom two held fixed to their lattice constant for Rh (3.8034 Å). The calculations on RhRe$_{201}$ clusters were carried out in a 30.4352 Å cubic unit cell to ensure a sufficient vacuum region to separate clusters in neighboring cells; all cluster atoms were allowed to relax in energy calculations and transition state searches. Transition state searches were performed using the dimer[42] method with the initial guesses for the transition state structure and the reaction trajectory obtained through the nudged elastic band method.[43]

■ ASSOCIATED CONTENT

ⓢ Supporting Information. Table of the effect of metal-loading ratio on catalytic activity and selectivity, table of the effect of pretreatment conditions on hydrogenolysis activity and Re leaching, table of hydrogenolysis rates and DFT-calculated carbenium and oxocarbenium ion energies, table of hydrogenolysis rates of **1** over 4 wt % Rh−ReO$_x$/C (1:0.5) in a continuous flow reaction system with varying reactant concentrations and P$_{H2}$, figure of DFT-calculated metal-catalyzed ring-opening of **3**, figure of DFT-optimized structure for water-stabilized tetrahydrofurfuryl carbenium ion transition state. This material is available free of charge via the Internet at http://pubs.acs.org.

■ AUTHOR INFORMATION

Corresponding Author
dumesic@engr.wisc.edu

■ ACKNOWLEDGMENT

■ REFERENCES

(1) Chheda, J. N.; Huber, G. W.; Dumesic, J. A. *Angew. Chem., Int. Ed.* **2007**, *46* (38), 7164−7183.

(2) Schlaf, M. *Dalton Trans.* **2006**, *39*, 4645−4653.

(3) Koso, S.; Furikado, I.; Shimao, A.; Miyazawa, T.; Kunimori, K.; Tomishige, K. *Chem. Commun.* **2009**, *15*, 2035−2037.

(4) Chen, K.; Koso, S.; Kubota, T.; Nakagawa, Y.; Tomishige, K. *ChemCatChem* **2010**, *2* (5), 547−555.

(5) Nakagawa, Y.; Shinmi, Y.; Koso, S.; Tomishige, K. *J. Catal.* **2010**, *272* (2), 191−194.

(6) Ma, L.; He, D. *Catal. Today* **2009**, *149* (1−2), 148−156.

(7) Ma, L.; He, D.; Li, Z. *Catal. Commun.* **2008**, *9* (15), 2489−2495.

(8) Daniel, O. M.; DeLaRiva, A.; Kunkes, E. L.; Datye, A. K.; Dumesic, J. A.; Davis, R. J. *ChemCatChem* **2010**, *2* (9), 1107−1114.

(9) Gault, F. G.; Eley, D. D.Pines, H.Weisz, P. B., Eds. Mechanisms of skeletal isomerization of hydrocarbons on metals. In *Advances in Catalysis*; Academic Press: New York, 1981; Vol. 30; pp 1−95.

(10) Koso, S.; Ueda, N.; Shinmi, Y.; Okumura, K.; Kizuka, T.; Tomishige, K. *J. Catal.* **2009**, *267* (1), 89−92.

(11) Kip, B. J.; Hermans, E. G. F.; Van Wolput, J. H. M. C.; Hermans, N. M. A.; Van Grondelle, J.; Prins, R. *Appl. Catal.* **1987**, *35* (1), 109−139.

(12) Van 'T Blik, H. F. J.; Niemantsverdriet, J. W. *Appl. Catal.* **1984**, *10* (2), 155−162.

(13) Reyes, P.; Concha, I.; Pecchi, G.; Fierro, J. L. G. *J. Mol. Catal. A: Chem.* **1998**, *129* (2−3), 269−278.

(14) Simonetti, D. A.; Kunkes, E. L.; Dumesic, J. A. *J. Catal.* **2007**, *247* (2), 298−306.

(15) Augustine, S. M.; Sachtler, W. M. H. *J. Catal.* **1989**, *116* (1), 184−194.

(16) Kunkes, E. L.; Simonetti, D. A.; Dumesic, J. A.; Pyrz, W. D.; Murillo, L. E.; Chen, J. G.; Buttrey, D. J. *J. Catal.* **2008**, *260* (1), 164−177.

(17) Kunimori, K.; Uchijima, T.; Yamada, M.; Matsumoto, H.; Hattori, T.; Murakami, Y. *Appl. Catal.* **1982**, *4* (1), 67−81.

(18) Gatica, J. M.; Baker, R. T.; Fornasiero, P.; Bernal, S.; Blanco, G.; Kašpar, J. *J. Phys. Chem. B* **2000**, *104* (19), 4667−4672.

(19) Halttunen, M. E.; Niemelä, M. K.; Krause, A. O. I.; Vaara, T.; Vuori, A. I. *Appl. Catal., A* **2001**, *205* (1−2), 37−49.

(20) Sharma, S. B.; Meyers, B. L.; Chen, D. T.; Miller, J.; Dumesic, J. A. *Appl. Catal., A* **1993**, *102* (2), 253−265.

(21) Niwa, M.; Katada, N.; Sawa, M.; Murakami, Y. *J. Phys. Chem.* **1995**, *99* (21), 8812−8816.

(22) Cardona-Martinez, N.; Dumesic, J. A., Thermochemical Characterization. In *Handbook of Heterogeneous Catalysis*; Wiley-VCH Verlag GmbH & Co. KGaA: Weinheim, 2008; pp 1122−1135.

(23) Janik, M. J.; Macht, J.; Iglesia, E.; Neurock, M. *J. Phys. Chem. C* **2009**, *113* (5), 1872−1885.

(24) Macht, J.; Janik, M. J.; Neurock, M.; Iglesia, E. *J. Am. Chem. Soc.* **2008**, *130* (31), 10369−10379.

(25) Janik, M. J.; Davis, R. J.; Neurock, M. *Catal. Today* **2005**, *105* (1), 134−143.

(26) Gennari, U.; Kramer, R.; Gruber, H. L. *Appl. Catal.* **1984**, *11* (2), 341−351.

(27) Gennari, U.; Kramer, R.; Gruber, H. L. *Appl. Catal.* **1988**, *44*, 239−250.

(28) Boudart, M.; Djega-Mariadassou, G. *Kinetics of Heterogeneous Catalytic Reactions*; Princeton University Press: Princeton, NJ, 1984; pp 114−116.

(29) Brändle, M.; Sauer, J. *J. Am. Chem. Soc.* **1998**, *120* (7), 1556−1570.

(30) King, D. L.; Zhang, L.; Xia, G.; Karim, A. M.; Heldebrant, D. J.; Wang, X.; Peterson, T.; Wang, Y. *Appl. Catal., B* **2010**, *99* (1−2), 206−213.

(31) Shinmi, Y.; Koso, S.; Kubota, T.; Nakagawa, Y.; Tomishige, K. *Appl. Catal., B* **2010**, *94* (3−4), 318−326.

(32) Ma, L.; He, D. H. *Top. Catal.* **2009**, *52* (6−7), 834−844.

(33) Spiewak, B. E.; Shen, J.; Dumesic, J. A. *J. Phys. Chem.* **1995**, *99* (49), 17640−17644.

(34) Delley, B. *J. Chem. Phys.* **1990**, *92* (1), 508−517.

(35) *MaterialStudio*, V. 4.0; Accelrys, Inc.: San Diego, CA, 2010.

(36) Perdew, J. P.; Chevary, J. A.; Vosko, S. H.; Jackson, K. A.; Pederson, M. R.; Singh, D. J.; Fiolhais, C. *Phys. Rev. B* **1992**, *46* (11), 6671.

(37) Kresse, G.; Hafner, J. *Phys. Rev. B* **1994**, *49* (20), 14251.

12688

dx.doi.org/10.1021/ja2038358 |*J. Am. Chem. Soc.* 2011, 133, 12675–12689

(38) Kresse, G.; Furthmüller, J. *Phys. Rev. B* **1996**, *54* (16), 11169.

(39) Kresse, G.; Furthmüller, J. *Comput. Mater. Sci.* **1996**, *6* (1), 15–50.

(40) Vanderbilt, D. *Phys. Rev. B* **1990**, *41* (11), 7892.

(41) Monkhorst, H. J.; Pack, J. D. *Phys. Rev. B* **1976**, *13* (12), 5188.

(42) Graeme, H.; Hannes, J. *J. Chem. Phys.* **1999**, *111* (15), 7010–7022.

(43) Jonsson, H.; Mills, G.; Jacobsen, K. W., *Nudged Elastic Band Method for Finding Minimum Energy Paths of Transitions*; World Scientific: Singapore, 1998.